Journal of Colloid and Interface Science 662 (2024) 11–18

Contents lists available at ScienceDirect

Journal of Colloid And Interface Science

journal homepage: www.elsevier.com/locate/jcis

Size-independent boosting of near-infrared persistent luminescence in nano-phosphors via a magnesium doping strategy

Li-Xia Yan [a,b,c], Zhu-Ying Yan [f], Xu Zhao [a,b,c], Li-Jian Chen [a,b,c], Tian-Xi Liu [d,e], Xiu-Ping Yan [a,b,c,d,*]

[a] State Key Laboratory of Food Science and Resources, Jiangnan University, Wuxi 214122, China
[b] International Joint Laboratory on Food Safety, Jiangnan University, Wuxi 214122, China
[c] Institute of Analytical Food Safety, School of Food Science and Technology, Jiangnan University, Wuxi 214122, China
[d] Key Laboratory of Synthetic and Biological Colloids, Ministry of Education, Jiangnan University, Wuxi 214122, China
[e] School of Chemical and Material Engineering, International Joint Research Laboratory for Nano Energy Composites, Jiangnan University, Wuxi 214122, China
[f] Analysis and Testing Center, Jiangnan University, Wuxi 214122, China

GRAPHICAL ABSTRACT

Table of Contents

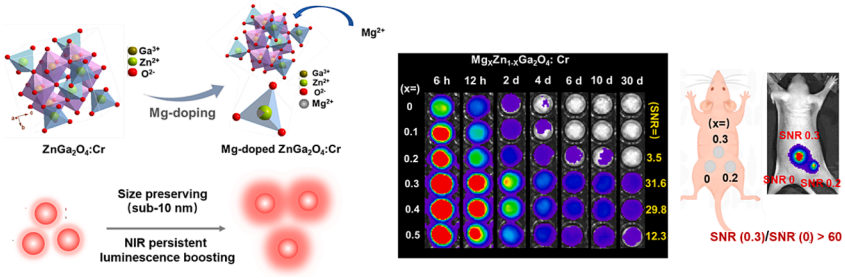

ARTICLE INFO

Keywords:
Persistent luminescence nanoparticles
Long-term bioimaging
Near-infrared luminescence
Optical imaging

ABSTRACT

Near-infrared (NIR)-emitting persistent luminescence nanoparticles (PLNPs) are ideal optical imaging contrast reagents characterized by autofluorescence-free optical imaging for their frontier applications in long-term bioimaging. Preparation of uniform small-sized PLNPs with excellent luminescence performance is crucial for biomedical applications, but challenging. Here, we report a facile magnesium doping strategy to achieve size-independent boost of NIR persistent luminescence in typical and most concerned $ZnGa_2O_4:Cr^{3+}$ PLNPs. This strategy relies on the doping of Mg^{2+} ions that with similar size of Zn^{2+} ions in the host lattice matrix, and concomitant to the electron traps tailoring tuned by varying the feed ratio of Mg^{2+}. The optimum Mg^{2+}-doped PLNPs give a long afterglow time (signal-to-noise ratio (SNR) = 31.6 at 30 d) without changing the desirable uniform sub-10 nm size of the original nanocrystals. The appropriate increase of the depth and concentration of electron trap contribute jointly to the enhancement of lifetime (488 % longer, 20.57 s) and afterglow time for 700 nm persistent luminescence. Meanwhile, these PLNPs keep the original excellent rechargeability and

* Corresponding author at: State Key Laboratory of Food Science and Resources, Jiangnan University, Wuxi 214122, China.
E-mail address: xpyan@jiangnan.edu.cn (X.-P. Yan).

https://doi.org/10.1016/j.jcis.2024.02.008
Received 7 September 2023; Received in revised form 11 January 2024; Accepted 1 February 2024
Available online 6 February 2024
0021-9797/© 2024 Elsevier Inc. All rights reserved.

promote over 60 times increase of SNR in renewable in vivo imaging. This simple strategy provides a basis for new opportunities to address the critical challenge of effective optical performance boost in small-sized PLNPs.

1. Introduction

Persistent luminescence (PL) is a fascinating optical phenomenon with continuous light emission from minutes to days after the excitation source vanishes [1–3]. Such unique "self-sustained" luminescence property makes persistent luminescence nanoparticles (PLNPs) exceptional as ideal optical imaging contrast reagents in various biomedical applications [4–7]. Specifically, near-infrared (NIR) PLNPs enable significant improvement of signal-to-background ratio and sensitivity in bioimaging, ultrasensitive detection and long-term biomolecule tracking [2,8–11].

Preparation of high-quality PLNPs with both uniform small size and excellent persistent luminescence is crucial for their biomedical applications. Most early PLNPs were prepared by the "top-down" method to get nanometric size alternative after the bulky persistent phosphors were broken into nanoscale particles [1,2,12,13]. This method first needs solid-state annealing at high temperatures to get good afterglow performance of bulky persistent luminescence materials, and then generally requires a further mechanical milling process to deal with large sizes and serious aggregation. However, the uncontrollable mechanical milling method usually results in the broad size distribution, serious surface defect, unpredictable morphology and poor luminescence performance [14,15]. Moreover, such uncontrollable preparation dramatically restricts the potential in delicate chemistry and biology studies [16–18].

Great efforts have been made to develop "bottom-up" methods for the fabrication of PLNPs with controllable uniform size, such as solvothermal synthesis [2,18,19,20], templated synthesis [17,21,22] and sol–gel synthesis [7]. However, the afterglow luminescence of the prepared small-sized PLNPs is usually unsatisfactory due to the inadequate crystallinity at low reaction temperature and surface quenchers that come from larger surface-to-volume ratio. Smaller particles (<10 nm) are often employed for more precise labelling of cellular structures in practical imaging applications, while excellent PL performance is required to improve the imaging quality and detection sensitivity in long-term and deep tissue monitoring in vivo.

It is still difficult to prepare high-quality PLNPs with both uniform small size and excellent PL. Recent studies reveal that the afterglow enhancement of PLNPs ($Zn_{1+x}Ga_{2-2x}Ge_xO_4$: Cr^{3+}) was usually coupled with the dramatic increase of particle size in bottom-up synthesis [23–25]. Conventional high temperature calcination produces excellent PL, but unfavorable large-sized particles for biomedical applications. Moreover, low reaction temperature favors for the preparation of small-sized PLNPs, but usually creates inadequate crystallinity and excessive surface quenchers which inevitably sacrifice PL performance. For these reasons, it is very hard for previous studies to achieve ideal PLNPs which not only give excellent PL performance but also uniform small size [3,19,26]. Therefore, it remains a key challenge to boost the PL of PLNPs through bottom-up design but without sacrificing their size and uniformity.

Herein, we report a facile Mg^{2+} ions doping strategy to boost the PL of small-sized PLNPs without sacrificing the size and uniformity. As shown in Fig. 1, $ZnGa_2O_4$:Cr^{3+} is taken as model PLNPs because it has raised great interest as one of the most effective NIR PLNPs to date.

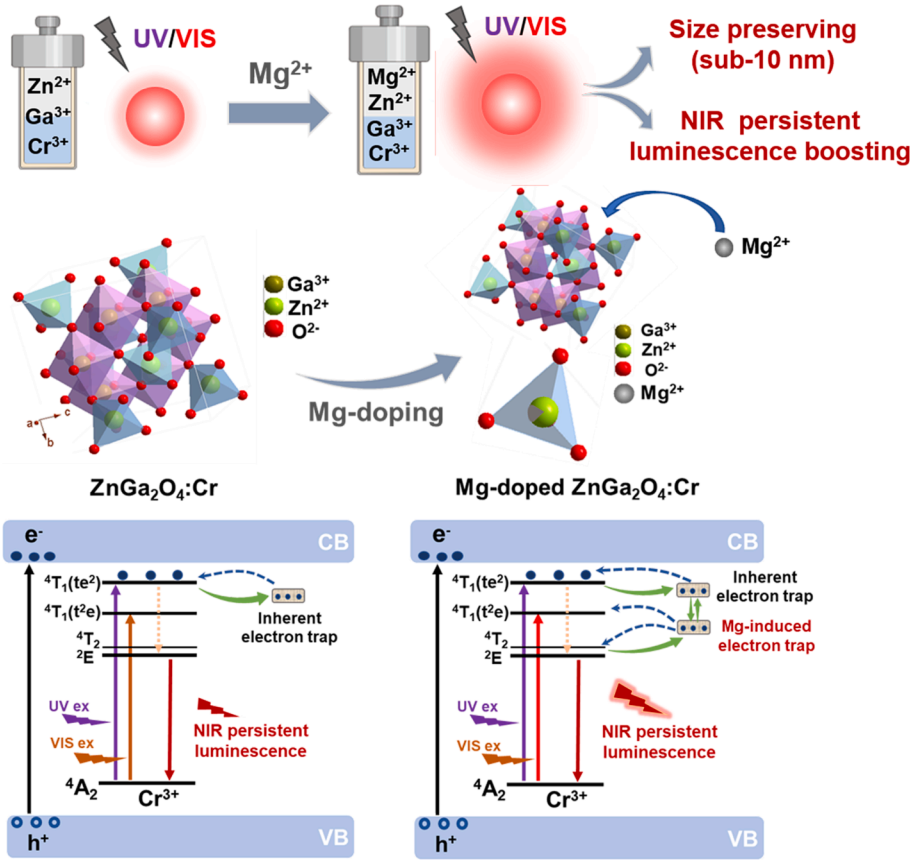

Fig. 1. Schematic illustration of the engineering electron traps in $ZnGa_2O_4$: Cr^{3+} nanoparticles through Mg-doping.

Magnesium ions (0.72 Å) is chosen to partial substitute zinc ions (0.74 Å) in $ZnGa_2O_4:Cr^{3+}$ due to their close size. The doping of Mg^{2+} ions is systematically tuned in mixed spinel, and the slight substitution of Zn^{2+} by Mg^{2+} gives a size-independent enhancement of PL intensity and afterglow decay time. The partial doping of Mg^{2+} ions in the nanocrystals produces more inherent electron traps and a new type of trap. The excellent afterglow performance of Mg-doped PLNP ($Mg_xZn_{1-x}Ga_2O_4:Cr^{3+}$) is further confirmed by renewable in vivo imaging. As such, we provide an efficient and facile ions doping strategy to address the critical challenge for effective PL boost with desirable size and morphology preservation of PLNPs.

2. Results and discussion

Preparation and Characterization of $Mg_xZn_{1-x}Ga_2O_4:Cr^{3+}$. To minimize the influence on the nanocrystal crystallization and keep the size and uniformity of original $ZnGa_2O_4:Cr^{3+}$, we proposed a facile strategy to substitute Zn^{2+} by close-sized Mg^{2+} in mixed spinel. Fig. 1. shows the schematic diagram for the developed Mg^{2+} doping strategy to boost the PL of small-sized PLNPs without sacrificing the size and uniformity. To show the effect of Mg^{2+} doping, we prepared a series of $Mg_xZn_{1-x}Ga_2O_4:Cr^{3+}$ PLNPs by tuning the doping of Mg^{2+} ions in the precursor solution. All the $Mg_xZn_{1-x}Ga_2O_4:Cr^{3+}$ ($0 \leq x \leq 0.5$) PLNPs were synthesized by a typical bottom-up hydrothermal method. In a typical preparation of optimized formula $Mg_xZn_{1-x}Ga_2O_4:Cr^{3+}$ ($x = 0.3$), 0.3 mmol Mg^{2+}, 0.7 mmol Zn^{2+}, 2 mmol Ga^{3+}, 0.003 mmol Cr^{3+} were mixed, and the precursor ion were further precipitated in alkaline solution via hydro-thermal crystallization. The prepared $Mg_xZn_{1-x}Ga_2O_4:Cr^{3+}$ ($x = 0.3$) showed highly crystalline typical cubic spinel structure with spherical and monodispersed morphology as well as 7.3 ± 1.4 nm diameter (Fig. 2a,b,c), and gave a consistent NIR emission (at ~ 700 nm) with $ZnGa_2O_4:Cr^{3+}$ (Fig. S1), originating from the spin forbidden ^2E-$^4A_2$ transition of the distorted Cr^{3+} ions [1,20,27,28]. Moreover, the prepared $Mg_xZn_{1-x}Ga_2O_4:Cr^{3+}$ ($x = 0.3$) exhibited a significant enhancement of NIR persistent luminescence at ~ 700 nm with an average lifetime of 20.57 s and a long afterglow time (signal-to-noise ratio (SNR) = 31.6 at 30 d for the powder) (Fig. 3a,b,c).

Effect of Mg^{2+}-doping on Morphology, Size and Crystal Structure. To systematically investigate the effect of Mg^{2+}-doping, the size and crystal structure of the nanoparticles were studied using transmission electron microscopy (TEM) and X-ray powder diffraction (XRD). In the absence of Mg^{2+} ($x = 0$), the resulting $ZnGa_2O_4:Cr^{3+}$ nanoparticles were spherical and monodispersed with the diameter of 5.8 ± 1.3 nm ($n = 200$) (Fig. 2a,b). Mg-doping did not lead to significant change in the morphology and size of the nanoparticles (Fig. 2a,b, Fig. S2), and the nanoparticles are colloidally stable and monodispersed with a narrow hydrodynamic size distribution of 11.5 ± 5.0 nm (Fig. S3). In addition, atomic level substitution did not affect the hydrothermal crystallization of $Mg_xZn_{1-x}Ga_2O_4:Cr^{3+}$ significantly due to the quite close ionic radii of Mg^{2+} and Zn^{2+} ions. The prepared $Mg_xZn_{1-x}Ga_2O_4:Cr^{3+}$ ($x = 0$–0.5) nanocrystals gave a highly crystalline typical cubic spinel structure (JCPDS 38–1240), and displayed clear resolved lattice fringes corresponding to the 311 spacing of cubic spinel regardless of Mg-doping (Fig. 2c,d). However, the crystallinity in 311 crystal-plane gradually increased with the content of doped Mg^{2+} ions, maximizing at $x = 0.3$ (Fig. 2e). This is mainly due to the slight crystal lattice shrinkage arising from the substitution of Zn^{2+} by slightly smaller ionic radii Mg^{2+}. Elemental mapping analysis shows that the elements of Zn, Mg, Ga, O and Cr were evenly distributed in the nanoparticles after Mg-doping (Fig. 2f), indicating the solid solution nature of the nanocrystals and the effective doping of Mg^{2+} ions into $ZnGa_2O_4:Cr^{3+}$ crystal lattice. The above results show that the morphology, size and crystal structure of $ZnGa_2O_4:Cr^{3+}$ nanoparticles did not change significantly by Mg^{2+} ions doping.

Effect of Mg^{2+}-Doping on Optical Properties. High-efficiency activation of PLNPs with light is crucial for the restoration of PL in

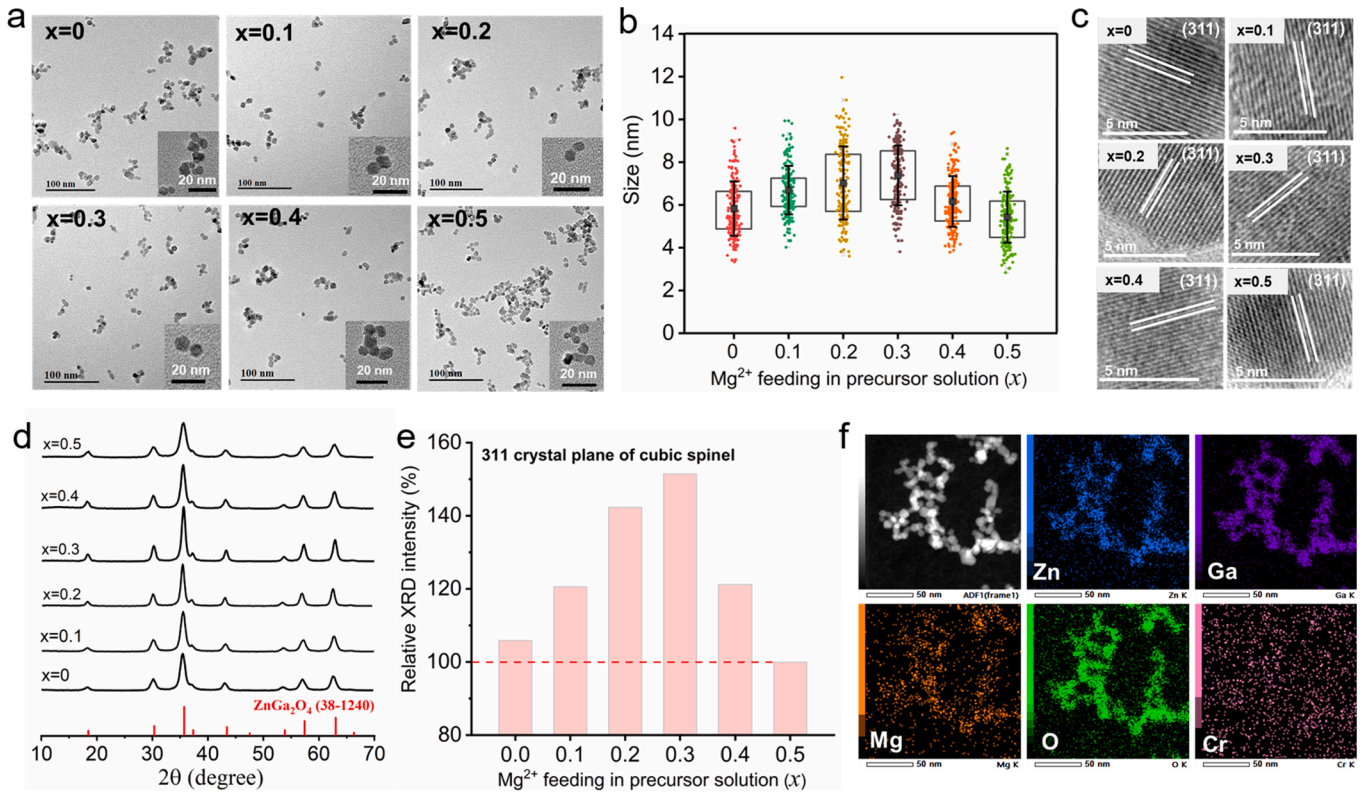

Fig. 2. Characterization of $Mg_xZn_{1-x}Ga_2O_4:Cr^{3+}$ ($x = 0$–0.5). (a) TEM images. (b) Size distribution ($n = 200$). (c) High-resolution TEM images. (d) X-ray diffraction (XRD) patterns of the magnesium-doped nanoparticles. (e) Relative intensity of the crystallinity in 311 crystal-plane of the nanoparticles. (f) EDS element mapping of $Mg_xZn_{1-x}Ga_2O_4:Cr^{3+}$ ($x = 0.1$).

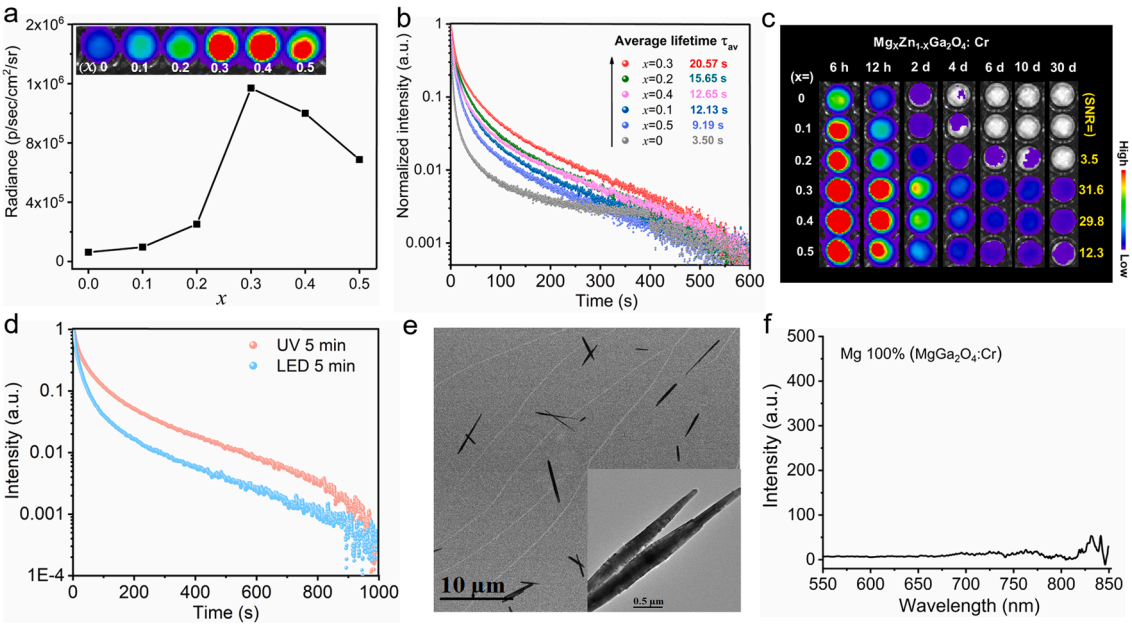

Fig. 3. Persistent luminescence properties of Mg-doped $ZnGa_2O_4:Cr^{3+}$. (a) PL decay images and corresponding PL quantification at 96 h after irradiation with a UV lamp for 5 min. (b) Normalized PL decay curve monitored at 700 nm after irradiation with a UV lamp (254 nm) for 5 min. The decay curves were recorded 15 s after excitation ceased. (c) NIR afterglow decay images of Mg-doped $ZnGa_2O_4:Cr^{3+}$ NPs recorded by CCD camera at different times after stopping UV irradiation. (d) PL decay curves of $Mg_xZn_{1-x}Ga_2O_4:Cr^{3+}$ (x = 0.3) excited by a UV lamp and LED light for 5 min. The decay curves were recorded 15 s after excitation ceased. Characterization of $MgGa_2O_4:Cr^{3+}$. (e) TEM images of $MgGa_2O_4:Cr^{3+}$. (f) Photoluminescence spectrum of $MgGa_2O_4:Cr^{3+}$.

vivo to improve long-term bioimaging sensitivity and signal-to-noise ratio. The PL emission intensity of PLNPs changed significantly, relying on the Mg^{2+} doping contents. $Mg_xZn_{1-x}Ga_2O_4:Cr^{3+}$ with x = 0.2 display about 2.2 times the amplified photoluminescence intensity compared to $ZnGa_2O_4:Cr^{3+}$ (Fig. S4). Importantly, the excitation peaks of PLNPs at about 260 nm remain similar (Fig. S5), indicating that the bandgaps of these nanocrystals are almost identical regardless of Mg^{2+} doping.

The impact of Mg^{2+}-doping on the persistent luminescence was then investigated. The as-synthesized $Mg_xZn_{1-x}Ga_2O_4:Cr^{3+}$ exhibited excellent long-lasting NIR luminescence. The Mg-doped nanocrystals gave enhanced luminescence intensity in NIR afterglow decay images and PL decay curves, maximizing at x = 0.3 (Fig. 3a, Fig. S6). Moreover, Mg^{2+}-doped PLNPs showed a slower decay in the PL decay curves with a maximum luminescence lifetime at x = 0.3 (Fig. 3b). The optimal average lifetime of Mg-doping PLNPs is 488 % longer than that of the nanocrystals without Mg-doping ($\tau_{av\ (x=0.3)} = 20.57$ s *vs* $\tau_{av\ (x=0)} = 3.50$ s) (Table S1 and S2). The NIR PL was still detectible with a SNR of 31.6 by a CCD camera for 30 days without the need for any external illumination (Fig. 3c). In addition, $Mg_xZn_{1-x}Ga_2O_4:Cr^{3+}$ (x = 0.3) NPs show excellent rechargeability for UV (254 nm)/visible (650 nm red LED light) radiation with reproducible decay cycles (Fig. 3d, Fig. S7). The direct activation by red LED light makes these nanoparticles more valuable in biomedical application. Collectively, the above results clearly show that properly Mg^{2+}-doping effectively boosted the PL intensity and lifetime of $ZnGa_2O_4:Cr^{3+}$, while kept the uniform sub-10 nm size.

It is noteworthy that excessive Mg^{2+} doping with x beyond 0.3 is detrimental to persistent luminescence in nanocrystals (Fig. 3a,c). As a matter of fact, we attempted to replace 100 % Zn^{2+} by Mg^{2+}, the resulting $MgGa_2O_4:Cr^{3+}$ nanocrystals looked micron-sized rodlike (Fig. 3e), but gave no photoluminescence signal (Fig. 3f). The above results indicate that the optimal amount of Zn^{2+} is essential for the nanocrystal formation and afterglow signal enhancement in Mg-doped $ZnGa_2O_4:Cr^{3+}$.

Mechanisms on Mg^{2+}-Doping Improved PL Performance. To figure out the mechanisms on the effect of Mg^{2+}-doping on the PL performance of $ZnGa_2O_4:Cr^{3+}$ nanocrystals, the doped content of Mg^{2+} and the electron traps in the prepared PLNPs were further investigated. Fig. S8 shows that the doped Mg^{2+} content in $Mg_xZn_{1-x}Ga_2O_4:Cr^{3+}$ increased with the feeding amount of Mg^{2+} precursor. In particular, the doped content of Mg^{2+} in $Mg_xZn_{1-x}Ga_2O_4:Cr^{3+}$ (x = 0.3) was determined to be 0.0146 %, which is much smaller than the initial content of Mg^{2+} in the feeding precursors (2.84 %).

High-resolution XPS spectra for Mg 1s, Zn $2p_{3/2}$ and Ga $2p_{3/2}$ in $Mg_xZn_{1-x}Ga_2O_4:Cr^{3+}$ were further analyzed to reveal the effect of Mg^{2+}-doping on the local microstructure and the changing trends of occupation. The spectra of Mg 1s core levels exhibit asymmetric characteristics, and can be well fitted by bi-Gaussian function. The fitting binding energies at ~ 1300 eV and 1304 eV are assigned to the Mg^{2+} occupying tetrahedral sites and octahedral sites, respectively, because the cations occupying tetrahedral sites usually contributed to the smaller binding energy than those in the octahedral sites [29]. The XPS spectra of Mg 1s clearly shows that more Mg^{2+} occupied the tetrahedral sites as x increased from 0.1 to 0.5 (Fig. 4a, Table S3), confirming the slight substitution of Zn^{2+} by Mg^{2+}. Meanwhile, the percentage for the peak area assigned to tetrahedral sites gradually decreased in the spectra of Zn $2p_{3/2}$ due to the substitution of Zn^{2+} by Mg^{2+}, getting asymmetric spectra of Zn $2p_{3/2}$ core levels with Mg-doping (Fig. 4b, Table S4). Besides, the symmetric spectra of Ga $2p_{3/2}$ core levels for each sample can be fitted by a single Gaussian function (Fig. S9, Table S5), indicating that Ga^{3+} ions mainly occupy the octahedral sites.

The afterglow performance of Mg-doped $ZnGa_2O_4$ nanocrystals without Cr^{3+} doping was further studied to investigate the effect of Mg^{2+}-doping on the host lattices matrix of $ZnGa_2O_4$. The characteristic afterglow of Cr-free $ZnGa_2O_4$ nanocrystals was entirely from host matrix defects rather than the emission from Cr^{3+}. As a result, albeit being much weaker in intensity, the afterglow of Mg-doped $ZnGa_2O_4$ varied with the doped content of Mg^{2+} (x) in a similar way as that of Mg-doped $ZnGa_2O_4:Cr^{3+}$. Both chromium-free Mg-doped $ZnGa_2O_4$ and Mg-doped $ZnGa_2O_4:Cr^{3+}$gave the maximum PL emission intensity in PL spectra at a Mg/Zn molar ratio of 1:4 (i.e. x = 0.2) (Fig. 4c, Fig. S10), and the maximum afterglow intensity in NIR afterglow decay images at a Mg/Zn molar ratio of 3:7 (i.e. x = 0.3) (Fig. 4d,e). The consistent optical

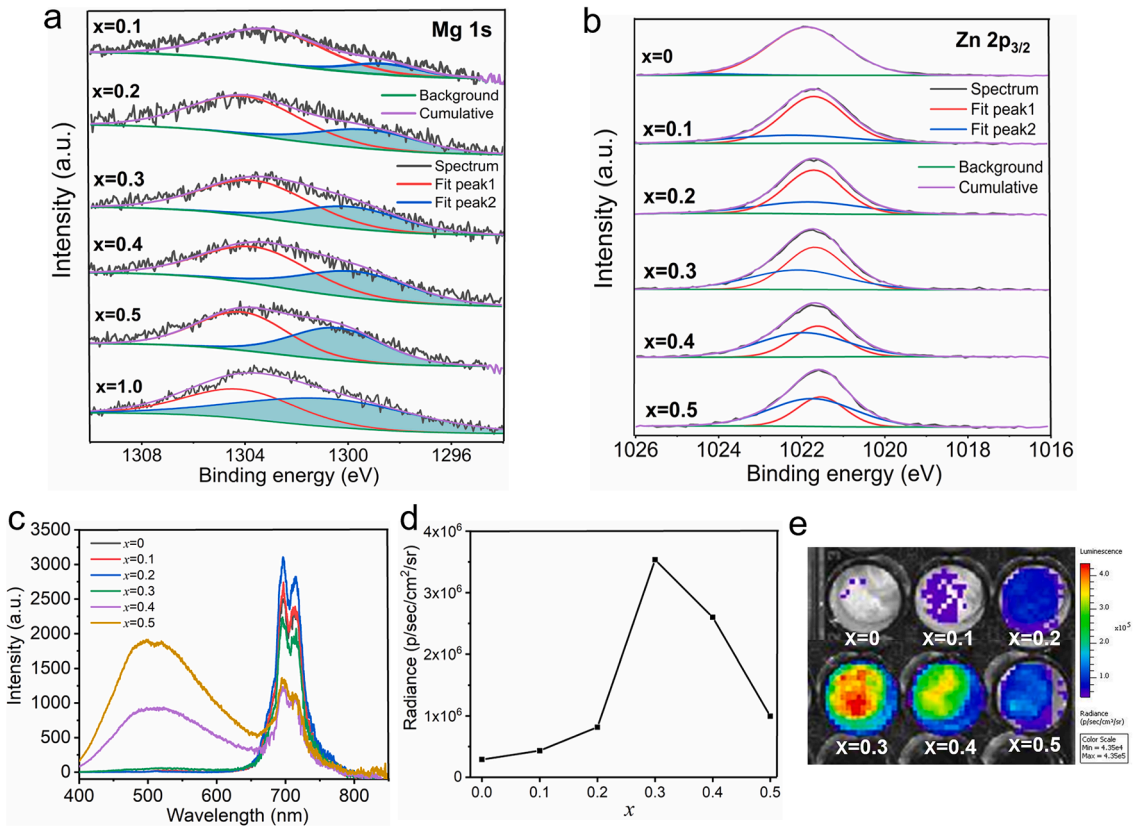

Fig. 4. Effect of Mg^{2+}-doping on the microstructure of $ZnGa_2O_4:Cr^{3+}$ nanoparticles. (a) High-resolution XPS spectra of Mg 1s core-levels for $Mg_xZn_{1-x}Ga_2O_4:Cr^{3+}$ nanocrystals (x = 0.1–0.5 and x = 1.0 (i.e. $MgGa_2O_4:Cr^{3+}$)). (b) High-resolution XPS spectra of Zn $2p_{3/2}$ core-levels for $Mg_xZn_{1-x}Ga_2O_4:Cr^{3+}$ (x = 0 (i.e. $ZnGa_2O_4:Cr^{3+}$) and x = 0.1–0.5) PLNPs. (c) Photoluminescence spectrum of the Cr-free $Mg_xZn_{1-x}Ga_2O_4$ nanoparticles with x from 0 to 0.5. (d) Quantification of luminescence intensity and (e) corresponding PL decay images of Cr-free $Mg_xZn_{1-x}Ga_2O_4$ powder at 48 h after irradiation with a UV lamp for 5 min.

performance in Mg-doped $ZnGa_2O_4:Cr^{3+}$ and Mg-doped Cr-free $ZnGa_2O_4$ nanocrystals suggests that the afterglow enhancement resulted from the effect of Mg^{2+} doping on the crystal-field environment of the host lattices matrix of $ZnGa_2O_4$ nanocrystals.

Thermoluminescence (TL) spectra was further studied to understand the mechanism. TL measurement is a versatile tool to investigate the properties and distribution of the electron traps in phosphors [30]. For $ZnGa_2O_4:Cr^{3+}$ nanocrystals without Mg-doping, there is an original TL peak at approximately 307 K (Fig. 5a). However, the intensity of the original TL peak multiply increased in Mg-doped nanocrystals, indicating the increased concentration of inherent electron traps. Moreover, the TL peak involved with intrinsic electron trap slightly shifted with Mg-doping (307, 317, 314, 325, 330, and 320 K for $Mg_xZn_{1-x}Ga_2O_4:Cr^{3+}$ with x = 0–0.5, respectively). Interestingly, Mg-doping led to a newly emerging peak at approximately 495 K. The new peak emerged its maximum with x = 0.1, and then decreased with the doping content increasement of magnesium. However, $Mg_xZn_{1-x}Ga_2O_4:Cr^{3+}$ with x = 0.3 gave the optimal luminescence lifetime and maximum luminescence intensity in the foregoing PL decay curves. It mainly due to that inadequate or excessive concentration and depth of electron traps is detrimental to afterglow performance. Considering the crucial role of concentration and depth of electron traps in the afterglow mechanisms, we further contrast the integrated area under the curve of TL intensity (299 K to 450 K), which reflects the concentration of the shallow

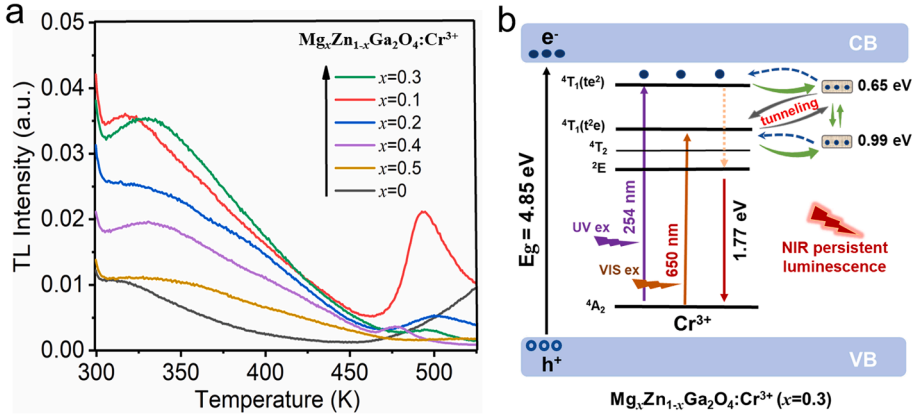

Fig. 5. Effect of Mg^{2+}-doping on the electron traps of $ZnGa_2O_4:Cr^{3+}$ nanoparticles. (a) Thermoluminescence spectra of Mg^{2+}-doped $ZnGa_2O_4:Cr^{3+}$ nanoparticles. (b) Diagram for engineering electron traps in $ZnGa_2O_4:Cr^{3+}$ nanoparticles through Mg-doping.

electron trap. We found that $Mg_xZn_{1-x}Ga_2O_4:Cr^{3+}$ with x = 0.3 gave the highest concentration of inherent electron trap (Table 1). Hence, the optimal long-lasting NIR luminescence of $Mg_xZn_{1-x}Ga_2O_4:Cr^{3+}$ (x = 0.3) was likely attributed to adequate shallow trap concentration and appropriate deep trap concentration in nanocrystals. The two peaks of $Mg_xZn_{1-x}Ga_2O_4:Cr^{3+}$ (x = 0.3) at about 325 K and 495 K correspond to two electron traps with a depth of $E_{trap1} \sim 0.65$ eV and $E_{trap2} \sim 0.99$ eV, respectively (according to the equation Et (eV) = $T_m/500$, T_m refers to the temperature at the TL peak maximum [31]) (Fig. 5b). Typically, traps with a medium depth of 0.5–1 eV, ideally around 0.65 eV are suitable for progressive release of carriers at room temperature, while shallower traps may lead to rapid afterglow decays and deeper ones to energy storage without release at room temperature [15,32]. In addition, the photo-charging effect curves under 254 nm UV light irradiation show the longest time needed to reach stable luminescence for $Mg_xZn_{1-x}Ga_2O_4:Cr^{3+}$ (x = 0.3), indicating that the trap level of the nanoparticles has a longer process from filling to release. This is consistent with the appropriate trap level and the observed optimal long-lasting NIR luminescence of $Mg_xZn_{1-x}Ga_2O_4:Cr^{3+}$ (x = 0.3) (Fig. S11). In brief, the appropriate Mg-doping not merely contributes the increased amount of inherent shallower electron traps, but also introduces a new type of deeper electron trap in the nanocrystals. These appropriate trap depth and trap concentration contribute jointly to the enhancement of afterglow performance.

The bandgap energy of $Mg_xZn_{1-x}Ga_2O_4:Cr^{3+}$ (x = 0–0.5) was estimated to investigate the physical origin of the NIR luminescence enhancement for specific Mg^{2+} ions doping levels. The reflectance spectra were used to calculate optical bandgap energy (Eg) by applying the Tauc plot, which was converted to the Kubelka-Munk function [33–35]. The calculated values of Eg were 4.94 eV (x = 0), 4.89 eV (x = 0.1), 4.81 eV (x = 0.2), 4.85 eV (x = 0.3), 4.82 eV (x = 0.4) and 4.83 eV (x = 0.5) (Fig. S12). The bandgap in $Mg_xZn_{1-x}Ga_2O_4:Cr^{3+}$ (x = 0.1–0.5) is slightly narrower as Mg^{2+} ions doping than that in the host sample (x = 0), meaning a more likely excitation of electrons from valence band to conduction band under the UV excitation. However, due to the small change in Eg, its contribution to the improvement of optical performance is limited.

We further considered the change of the inherent electron traps with Mg^{2+} doping to understand the mechanism. Based on the aforementioned results from the TL spectra, appropriate Mg-doping led to a significant increase of inherent shallower electron traps (Table 1). The long afterglow performance of Mg-doped $ZnGa_2O_4:Cr^{3+}$ under visible light excitation (red LED light, 650 nm) (Fig. 3d, Fig. S7) in combination with the linear time dependence of the reciprocal of the PL intensity indicate that a quantum tunneling-related process between trap and luminescent center were involved in the long persistent luminescence in Mg-doped phosphors (Fig. S13) [1,36,37]. The efficiency of the tunneling effect is related to the distance between the luminescent center and the trap center. The great increase of the concentration of inherent shallower electron traps by appropriate Mg-doping shortened the distance between the luminescence center and the trap center, thus the energy transfer efficiency from the material matrix to Cr^{3+} ions and the optical performance were significantly improved. The above physical origin analysis of the NIR luminescence enhancement can make good sense to explain the optimal luminescence lifetime and maximum luminescence duration of $Mg_xZn_{1-x}Ga_2O_4:Cr^{3+}$ (x = 0.3) (Fig. 5b).

We attempted to match this Mg^{2+} ions doping strategy to the green emitting Zn_2GeO_4:Mn PLNPs for further extend this strategy to other important PLNPs. However, Mg^{2+} doping (with x from 0.2 to 1.0) is detrimental to persistent luminescence in nanocrystals. The PL emission intensity of $Mg_xZn_{2-x}GeO_4$:Mn (~534 nm) significantly decrease relying on the Mg^{2+} doping contents (Fig. S14a), and the afterglow intensity and afterglow time of $Mg_xZn_{2-x}GeO_4$:Mn in afterglow decay images show the similar decrease trend (Fig. S14b-d). Therefore, this Mg^{2+} doping strategy needs to be further explored to match other important substrates of PLNPs.

Table 1
Integration of TL intensity from 299 K to 450 K

x Mg	0	0.1	0.2	0.3	0.4	0.5
Intergrated TL intensity (299 K to 450 K) (a.u.)	0.55	2.58	2.13	2.87	1.59	0.86

Persistent Luminescence Enhancement in In Vivo Imaging. In view of the good performance of light rechargeable Mg-doped PLNPs. We further investigated these nanoparticles with respect to their in vivo long-term imaging capability. For comparison, two groups of experiments were set up (UV lamp pre-activated group and LED in situ activated group). The nanoparticles in pre-activated group were irradiated by UV lamp for 5 min to fill the trap first, $Mg_xZn_{1-x}Ga_2O_4:Cr^{3+}$ solutions (x = 0, 0.2, 0.3) were subcutaneously injected into the same mouse on the back. The PL signal of the injected nanoparticles was then able to be continuously observed on an IVIS imaging system. The luminescence of Mg-doped PLNPs (x = 0.3) remained after 24 h of decay (SNR = 13.2), showing obviously improved PL signals compared to Mg-free PLNPs (x = 0) (Fig. 6a). Moreover, such improved PL signals of PLNPs was able to be quickly reactivated by red LED light, allowing the most simple and convenient recovery of the persistent luminescence signal whenever required.

To study the potential of the nanoparticles for bioimaging without UV lamp pre-activation, $Mg_xZn_{1-x}Ga_2O_4:Cr^{3+}$ in another group were directly excited by red LED light after subcutaneously injected. Decay images in Fig. 6b shows that the PL signal of Mg-doped PLNPs with x = 0.3 can keep at least 12 h (SNR = 13.7). Moreover, the repeated reactivation gave similar decay images without noticeable attenuation within 48 h, suggesting the good photostability of the Mg-doped PLNPs by red LED light (Fig. 6b, Fig. S15). In comparison with the $ZnGa_2O_4:Cr^{3+}$ (x = 0), the Mg-doped PLNPs (x = 0.3) promoted over 60 times increase of SNR in in vivo imaging. Besides, it is obviously that red light gave a better SNR than UV light. The above findings clearly demonstrate that properly Mg^{2+} ions doping in $ZnGa_2O_4:Cr^{3+}$ (x = 0.3) offered a significant improvement in vivo imaging performance, thus making the nanoparticles more valuable in long-term bioimaging.

3. Conclusion

We have developed a facile strategy ground on the direct aqueous bottom-up synthesis to boost the PL performance of $ZnGa_2O_4:Cr^{3+}$ PLNPs, while nicely preserving the desirable uniform sub-10 nm size and morphology. We have shown that the slight substitution of Zn^{2+} ions by Mg^{2+} ions in the nanocrystals led to increased amount of inherent electron traps and new deep electron traps. The appropriate depth and concentration of these added electron traps contribute jointly to the increase of PL intensity and duration of NIR emission (SNR = 31.6 at 30 d). Compared to previous studies [3,19,32], our proposed synthesis protocol allows the successful preparation of ideal PLNPs not only with excellent PL performance but also uniform small size. Moreover, the prepared nanocrystals exhibit excellent rechargeability for UV/visible radiations at a desired time, and promote over 60 times SNR increase in long-term in vivo bioimaging. The developed nanoparticles are ideal for autofluorescence free long-term bioimaging. Proper functionalization of the nanoparticles enables further develop promising nanoplatforms for disease diagnosis and long-term monitoring of physiological process.

CRediT authorship contribution statement

Li-Xia Yan: Writing – original draft, Methodology, Investigation, Data curation, Conceptualization. **Zhu-Ying Yan:** Methodology, Investigation. **Xu Zhao:** Validation, Methodology. **Li-Jian Chen:** Writing – original draft, Methodology, Investigation, Data curation, Conceptualization. **Tian-Xi Liu:** Supervision, Conceptualization. **Xiu-Ping Yan:** Writing – review & editing, Supervision, Funding acquisition,

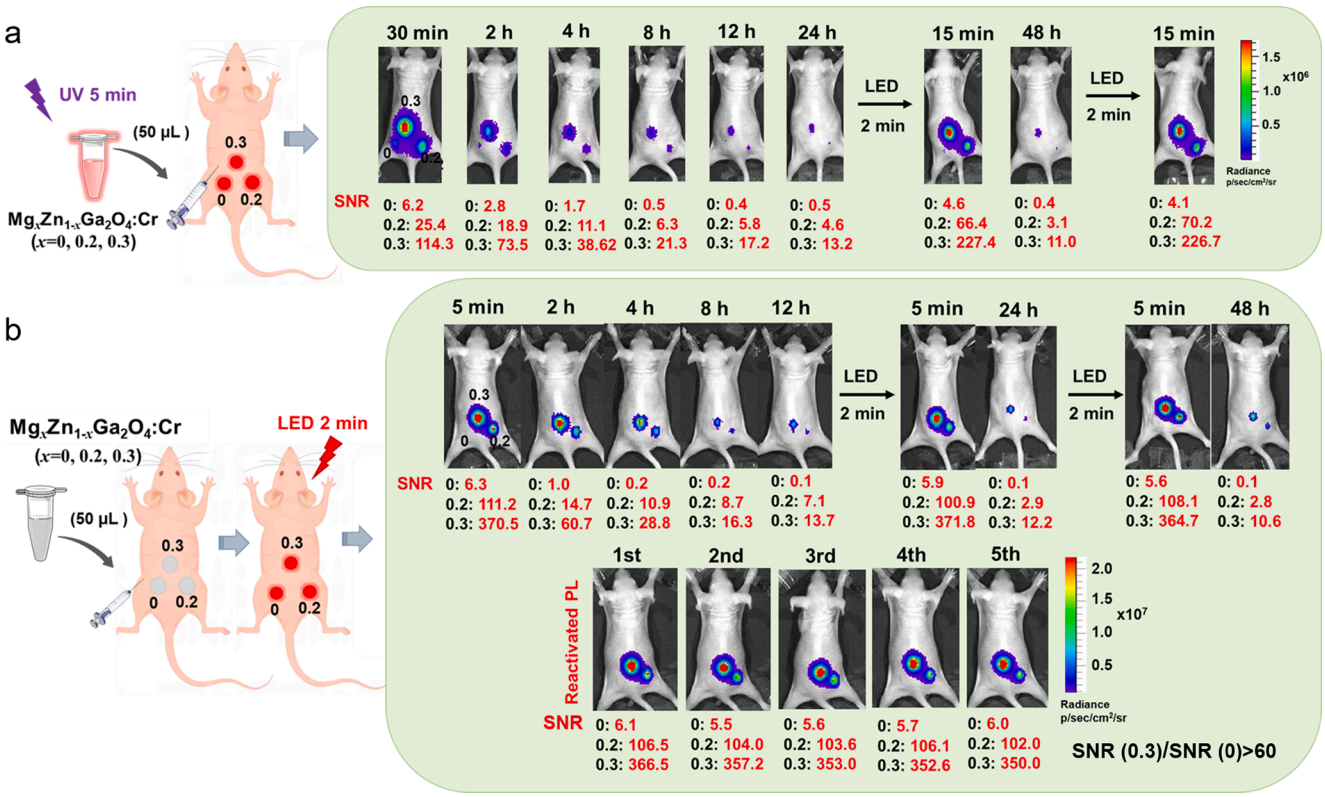

Fig. 6. Comparative in vivo imaging of normal mice after subcutaneous injection of $Mg_xZn_{1-x}Ga_2O_4:Cr^{3+}$ (x = 0, 0.2, 0.3) in PBS solution (50 μL, 4 mg mL^{-1}). The nanoparticles were pre-activated by UV lamp for 5 min before subcutaneous injection in one group (a), or (b) directly in situ activated and reactivated by LED light after subcutaneous injection but without UV lamp pre-activated in another group. NIR persistence photographs were recorded on IVIS Lumina III imaging system (Binning: 8; Exposure time: 60 s).

Conceptualization.

Declaration of competing interest

The authors declare that they have no known competing financial interests or personal relationships that could have appeared to influence the work reported in this paper.

Data availability

Data will be made available on request.

Acknowledgements

This work was supported by the National Natural Science Foundation of China (No. 21934002 and 22206060, 22304063), the Natural Science Foundation of Jiangsu Province, China (No. BK20231033).

Appendix A. Supplementary data

Supplementary data to this article can be found online at https://doi.org/10.1016/j.jcis.2024.02.008.

References

[1] Z. Pan, Y.-Y. Lu, F. Liu, Sunlight-activated long-persistent luminescence in the near-infrared from Cr3+-doped zinc gallogermanates, Nature Mater. 11 (2012) 58–63.
[2] S.K. Sun, H.F. Wang, X.P. Yan, Engineering persistent luminescence nanoparticles for biological applications: From biosensing/bioimaging to theranostics, *Acc. Chem. Res.* 51 (2018) 1131–1143.
[3] Y. Li, M. Gecevicius, J. Qiu, Long persistent phosphors-from fundamentals to applications, Chem. Soc. Rev. 45 (2016) 2090–2136.
[4] Y.J. Li, X.P. Yan, Synthesis of functionalized triple-doped zinc gal-logermanate nanoparticles with superlong near-infrared persistent luminescence for long-term orally administrated bioimaging, Nanoscale 8 (2016) 14965–14970.
[5] S. Wu, Y. Li, W. Ding, L. Xu, Y. Ma, L. Zhang, Recent advances of persistent luminescence nanoparticles in bioapplications, Nano-Micro Lett. 12 (2020) 70.
[6] B.Y. Wu, H.F. Wang, J.T. Chen, X.P. Yan, Fluorescence resonance energy transfer inhibition assay for α-fetoprotein excreted during cancer cell growth using functionalized persistent luminescence nanoparticles, J. Am. Chem. Soc. 133 (2011) 686–688.
[7] A. Abdukayum, J.T. Chen, Q. Zhao, X.P. Yan, Functional near infrared-emitting Cr3+/Pr3+ co-doped zinc gallogermanate persistent luminescent nanoparticles with superlong afterglow for in vivo targeted bioimaging, J. Am. Chem. Soc. 135 (2013) 14125–14133.
[8] K. Huang, N. Le, J.S. Wang, L. Huang, L. Zeng, W.-C. Xu, Z. Li, Y. Li, G. Han, Designing next generation of persistent luminescence: Recent advances in uniform persistent luminescence nanoparticles, Adv. Mater. 34 (2022) 2107962.
[9] L.-X. Yan, L.-J. Chen, X. Zhao, X.-P. Yan, Nanoplatform for in vivo persistent luminescence imaging and precise photothermal therapy of bacterial infection, Adv. Funct. Mater. 30 (2020) 1909042.
[10] B.-B. Wang, L.-X. Yan, L.-J. Chen, X. Zhao, X.-P. Yan, Responsive nanoplatform for persistent luminescence "turn-on" imaging and "on-demand" synergistic therapy of bacterial infection, J. Colloid. Interf. Sci. 610 (2022) 687–697.
[11] L.-X. Yan, B.-B. Wang, X. Zhao, L.-J. Chen, X.-P. Yan, A pH-responsive persistent luminescence nanozyme for selective imaging and killing of *Helicobacter pylori* and common resistant bacteria, ACS Appl. Mater. Interfaces. 13 (2021) 60955–60965.
[12] Q. le Masne de Chermont, C. Chanéac, J. Seguin, F. Pellé, S. Maîtrejean, J.-P. Jolivet, D. Gourier, M. Bessodes, D. Scherman, Nanoprobes with near-infrared persistent luminescence for in vivo imaging, Proc. Natl. Acad. Sci. U.S.A. 104 (2007) 9266–9271.
[13] T. Maldiney, A. Bessière, J. Seguin, E. Teston, S.K. Sharma, B. Viana, A.J.J. Bos, P. Dorenbos, M. Bessodes, D. Gourier, D. Scherman, C. Richard, The in vivo activation of persistent nanophosphors for optical imaging of vascularization, tumours and grafted cells, Nature Mater. 13 (2014) 418–426.
[14] M. Allix, S. Chenu, E. Véron, T. Poumeyrol, E.A. Kouadri-Boudjelthia, S. Alahrache, F. Porcher, D. Massiot, F. Fayon, Considerable improvement of long-persistent luminescence in germanium and tin substituted $ZnGa_2O_4$, Chem. Mater. 25 (2013) 1600–1606.
[15] M.N. da Silva, J.M. de Carvalho, M.C. de Abreu Fantini, L.A. Chiavacci, C. Bourgaux, Nanosized ZnGa2O4: Cr3+ spinels as highly luminescent materials for bioimaging, ACS Appl. Nano Mater. 2 (2019) 6918–6927.

[16] K. Huang, X. Dou, Y. Zhang, X. Gao, J. Lin, J. Qu, Y. Li, P. Huang, G. Han, Enhancing light and X-Ray charging in persistent luminescence nanocrystals for orthogonal afterglow anti-counterfeiting, Adv. Funct. Mater. 31 (2021) 2009920.
[17] J. Wang, Q. Li, H. Zhao, W. Yue, K. Zhang, X. Jiang, K. Li, Facile and controllable synthesis of the renal-clearable "Luminous Pearls" for in vivo afterglow/magnetic resonance imaging, ACS Nano 16 (2021) 462–472.
[18] X. Wei, X. Huang, Y. Zeng, L. Jing, W. Tang, X. Li, H. Ning, X. Sun, Y. Yi, M. Gao, Longer and stronger: improving persistent luminescence in size-tuned zinc gallate nanoparticles by alcohol-mediated chromium doping, ACS Nano 14 (2020) 12113–12124.
[19] Z. Li, Y. Zhang, X. Wu, L. Huang, D. Li, W. Fan, G. Han, Direct aqueous-phase synthesis of sub-10 nm "Luminous Pearls" with enhanced in vivo renewable near-infrared persistent luminescence, J. Am. Chem. Soc. 137 (2015) 5304–5307.
[20] Y. Wang, C.-X. Yang, X.-P. Yan, Hydrothermal and biomineralization synthesis of a dual-modal nanoprobe for targeted near-infrared persistent luminescence and magnetic resonance imaging, Nanoscale 9 (2017) 9049–9055.
[21] J. Wang, J. Li, J. Yu, H. Zhang, B. Zhang, Large hollow cavity luminous nanoparticles with near-infrared persistent luminescence and tunable sizes for tumor afterglow imaging and chemo-/photodynamic therapies, ACS Nano 12 (2018) 4246.
[22] J. Shi, X. Sun, S. Zheng, J. Li, X. Fu, H. Zhang, A new near-infrared persistent luminescence nanoparticle as a multifunctional nanoplatform for multimodal imaging and cancer therapy, Biomaterials 152 (2018) 15.
[23] J. Wang, Q. Ma, X.-X. Hu, H. Liu, W. Zheng, X. Chen, Q. Yuan, W. Tan, Autofluorescence-free targeted tumor imaging based on luminous nanoparticles with composition-dependent size and persistent luminescence, ACS Nano 11 (2017) 8010–8017.
[24] K. Huang, M. Jayakumar, Y. Zhang, Lutetium doping for making big core and core-shell upconversion nanoparticles, J. Mater. Chem. C 3 (2015) 10267–10272.
[25] S. Han, R. Deng, X. Xie, X. Liu, Enhancing luminescence in lanthanide-doped upconversion nanoparticles, Angew. Chem., Int. Ed. 53 (2014) 11702–11715.
[26] L. Liang, J. Chen, K. Shao, X. Qin, Z. Pan, X. Liu, Controlling persistent luminescence in nanocrystalline phosphors, Nat. Mater. 22 (2023) 289–304.
[27] A.L. Bessière, S.K. Sharma, N. Basavaraju, K.R. Priolkar, L. Binet, B. Viana, A.J. Bos, T. Maldiney, C. Richard, D. Scherman, Storage of visible light for long-lasting phosphorescence in chromium-doped zinc gallate, Chem. Mater. 26 (2014) 1365–1373.
[28] A. Bessière, S. Jacquart, K. Priolkar, A. Lecointre, B. Viana, D. Gourier, ZnGa2O4: Cr3+: a new red long-lasting phosphor with high brightness, Opt. Express. 19 (2011) 10131–10137.
[29] Z. Gong, Y. Liu, J. Yang, D. Yan, H. Zhu, C. Liu, C. Xu, H. Zhang, A Pr3+ doping strategy for simultaneously optimizing the size and near infrared persistent luminescence of ZGGO: Cr3+ nanoparticles for potential bio-imaging, Phys. Chem. Chem. Phys. 19 (2017) 24513–24521.
[30] Y.H. Kim, P. Arunkumar, B.Y. Kim, S. Unithrattil, E. Kim, S.-H. Moon, J.Y. Hyun, K. H. Kim, D. Lee, J.-S. Lee, W.B. Im, A Zero-Thermal-Quenching Phosphor, *Nature Mater.* 16 (2017) 543–550.
[31] S. Li, Y. Liu, C. Liu, D. Yan, H. Zhu, C. Xu, L. Ma, X. Wang, Improvement of X-ray storage properties of C12A7:Tb3+ photo-stimulable phosphors through controlling encaged anions, J. Alloy. Compd. 696 (2017) 828–835.
[32] V. Castaing, E. Arroyo, A.I. Becerro, M. Ocaña, G. Lozano, H. Míguez, Persistent luminescent nanoparticles: Challenges and opportunities for a shimmering future, J. Appl. Phys. 130 (2021) 080902.
[33] Y. Katayama, T. Kayumi, J. Ueda, S. Tanabe, Enhanced persistent red luminescence in Mn2+-doped (Mg, Zn) GeO3 by electron trap and conduction band engineering, Opt. Mater. 79 (2018) 147–151.
[34] J. Tauc, R. Grigorovici, A. Vancu, Optical Properties and Electronic Structure of Amorphous Germanium, Phys. Status Solidi. 15 (1966) 627–637.
[35] Y. Katayama, T. Kayumi, J. Ueda, P. Dorenbos, B. Viana, S. Tanabe, The role of Ln3+ (Ln=Eu, Yb) in persistent red luminescence in MgGeO3:Mn2+, J. Mater. Chem. C 5 (2017) 8893–8900.
[36] H. Guo, Y. Wang, W. Chen, W. Zeng, S. Han, G. Li, Y. Li, Controlling and revealing the trap distributions of Ca6BaP4O17:Eu2+, R3+ (R = Dy, Tb, Ce, Gd, Nd) by codoping different trivalent lanthanides, J. Mater. Chem. C 3 (2015) 11212–11218.
[37] Z. Zou, C. Cao, T. Zhang, L. Feng, J. Zhang, Z. Ci, Z. Zhang, Y. Wang, Structure, long persistent luminescent properties and mechanism of a novel efficient red emitting Ca2Ga2GeO7:Pr3+ phosphor, J. Alloy. Compd. 680 (2016) 397–405.